Modal Survey of the PACOSS DTA

Russell N Gehling

Martin Marietta Space Systems
Denver, Colorado

Abstract

Many future space systems will be constructed of large, flexible structures and will possess high modal density at low frequencies. Some missions envisioned for these large space systems (LSS) require rapid retargeting and precision pointing which lead to control bandwidths overlapping several structural modes. Therefore, some form of structural control will be necessary to avoid excessive excitation of the flexible modes. The purpose of passive/active damping is to allow the system to efficiently meet its performance goals.

The Passive and Active Control of Space Structures (PACOSS) program investigated the accuracy and practicality of designing and implementing passive damping in structures typical of many LSS configurations. This involved design and fabrication of a passively damped Dynamic Test Article (DTA) possessing high modal density at low frequencies. Also, an active modal damping system was designed and implemented. In order to verify the design methodology and effectiveness, a comprehensive modal survey was conducted on the DTA to identify flexible modes in the 1 to 10 Hz range. This paper discusses the modal survey, modal parameter identification, and comparison of measured and analytic results.

Modal parameter identification proved to be difficult for several DTA modes in the frequency range of interest. While the identified natural frequencies were quite repeatable, damping ratios and mode shapes tended to exhibit scatter on the order of 20% about the average, depending on the particular measurement and curve fit parameters. The difficulties were traced to both the highly damped, closely spaced nature of the modes and, to some extent, the data quality. Although parameter identification was inconsistent in some instances, the overall correlation between the test results and analytic predictions was quite good. Tests with the active modal damping system turned on (closed loop) were also conducted. Measured results were compared with corresponding analytic predictions of the control system performance and the system functioned as predicted, working in concert with the passive damping design.

Important conclusions may be drawn from the results of the DTA modal survey. Of most significance is the fact that predictable levels of passive damping can be designed into complex LSS-type structures. Also, the achievable damping levels significantly improve performance such as LOS settling time. Testing of the DTA revealed the need for study and application of more robust parameter identification algorithms to systems possessing highly damped, closely spaced modes.

INTRODUCTION

The ultimate goal of the PACOSS program was to demonstrate the synergistic benefit of passive damping working in concert with active vibration damping as applied to large space systems. Demonstration and verification of the technology required development of the Dynamic Test Article (DTA) pictured in Figure 1. The DTA is dynamically traceable to future large space systems through the Representative System Article (RSA) described in Reference 1, and depicted in Figure 2. A methodology for passive/active control design and its application to the RSA is presented in Reference 2. Details of the design and analysis of the several DTA substructures are given in Reference 3. Following fabrication, fixed interface modal surveys were conducted on each substructure. Results from these tests are discussed in Reference 4. An important aspect of system traceability is the presence of high modal density. In order to verify the high modal density of the DTA, and measure the accuracy and effectiveness of the damping design methodology, a modal survey was conducted on the DTA. This paper presents the results of the DTA modal survey and analytic modal analysis.

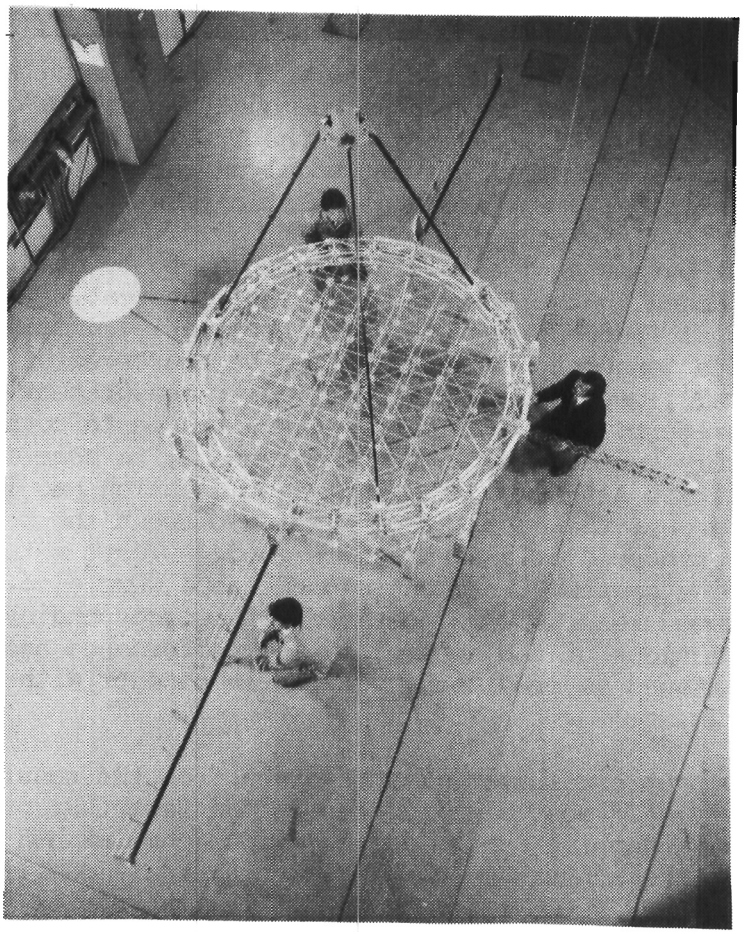

Figure 1 PACOSS Dynamic Test Article (DTA)

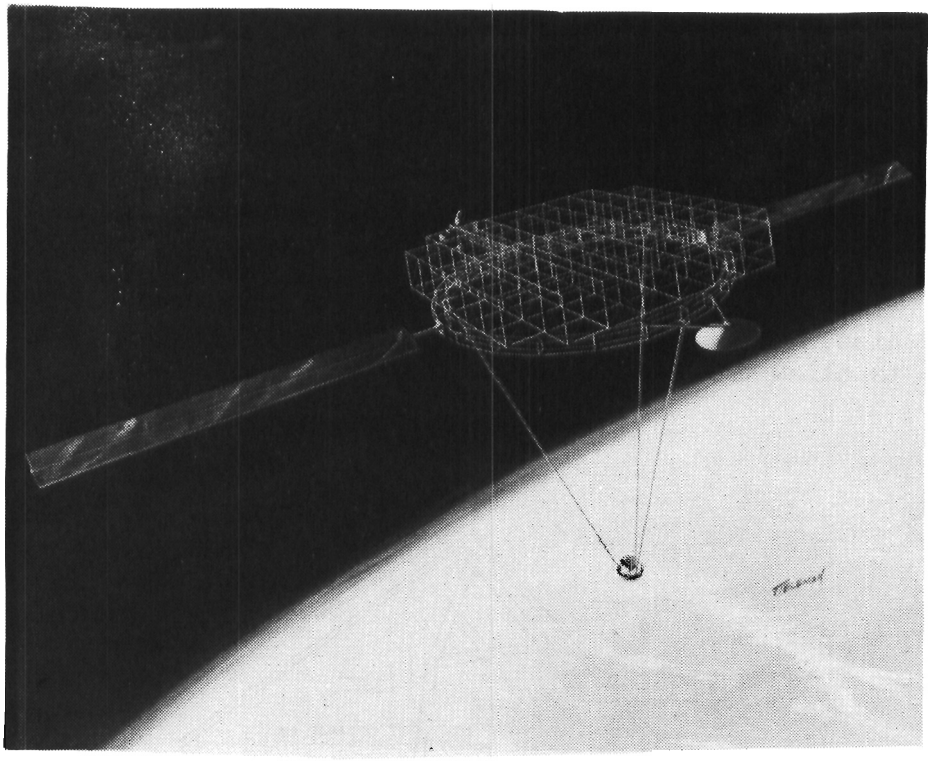

Figure 2 PACOSS Representative System Article (RSA)

TEST SETUP

The modal survey of the DTA generally followed the initial test plan. However, preliminary investigations, test modifications, and additional shaker configurations were included as the testing progressed. These efforts were undertaken in an effort to assure that the best possible data, within equipment and time constraints, were acquired. The following paragraphs present a brief overview of the DTA modal survey setup and testing.

Setup for the DTA testing involved assembly of a temperature control chamber, erection of a support fixture, and assembly of the DTA. The overall test setup is diagramed in Figure 3. The temperature control chamber performed quite well throughout the DTA testing, although wide fluctuations of the temperature outside the chamber (65.F to 90.F) required that the air conditioner be on continuously. The air flow from the air conditioner was directed upwards and did not measurably disturb the DTA.

The primary goal of the DTA modal survey was accurate determination of the modal parameters (frequency, damping ratios, shapes) for flexible modes below 10 Hz. Also, the performance and effectiveness of the active damping system was to be accessed through measurement of the increase in damping it provided to selected DTA modes. The modal parameters were to be determined through curve fitting of frequency response functions generated by measuring an external force and the resulting accelerations at selected points on the structure.

Figure 4 shows the measurement point locations on the DTA. The large number of measurements were required in order to obtain a valid reduction of the analytic mass matrix for use in orthogonality products between the measured and predicted mode shapes. Also, measurements were included across component interface points to allow troubleshooting of interface stiffness if the need arose.

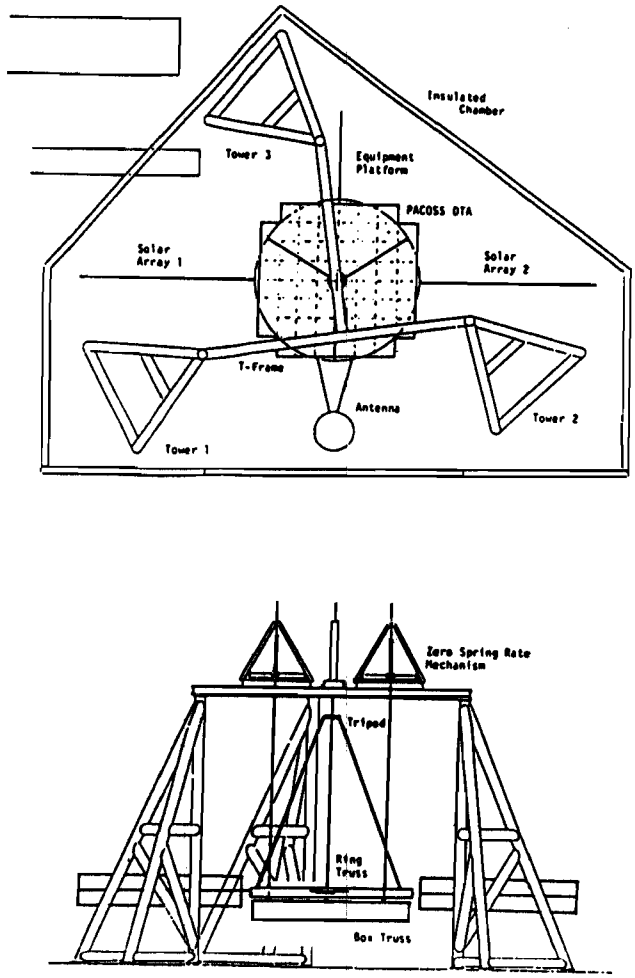

Figure 3 Modal Survey Setup

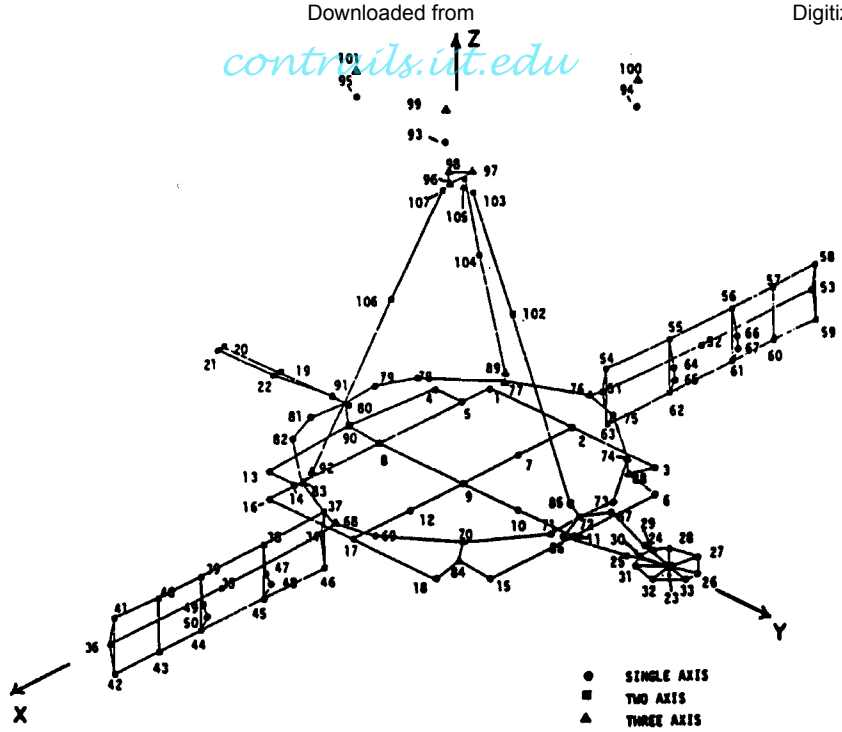

Figure 4 DTA Measurement Point Diagram

The relatively low frequency range of interest and the light weight of some DTA components required that shakers fixed to ground be used to excite the DTA. Suspending the shakers invariably resulted in coupling of the shaker suspension dynamics to the dynamics of the structure through rotational and lateral stiffness of the stinger in the 1 to 3 Hz range. However, in some instances, achieving a stiff shaker fixture with frequencies above 15 Hz was not possible. Also, the bending stiffness of the stinger can change the test article's behavior when attached to a fixed shaker. Therefore, swivel stingers with ball joints on each end were used to eliminate dynamic coupling of the shaker and DTA through rotational and lateral stinger stiffness. The platform which supported the shaker for excitation of the tripod top plate was a case where stinger stiffness allowed coupling of the platform dynamics to the DTA. Figure 5 dramatically demonstrates the effect on the drive point FRF of using a relatively stiff nylon stinger compared to the swivel stinger. The significant differences between the FRFs in the 3 to 6 Hz range are probably due to large rotational deflection of the tripod top plate for DTA modes in that frequency range. The same measurement was acquired using an impact hammer (no stinger involved) which, although noisy, verified the FRF acquired using the swivel stinger.

Figure 6 is a photo of the overall DTA test setup inside the thermal control chamber. Note the previously mentioned shaker support platform constructed around the tripod top plate visible at the top center of the photo. Previous testing of the components demonstrated that the many accelerometers cables hanging from the structure have no measurable effect of the DTA dynamics.

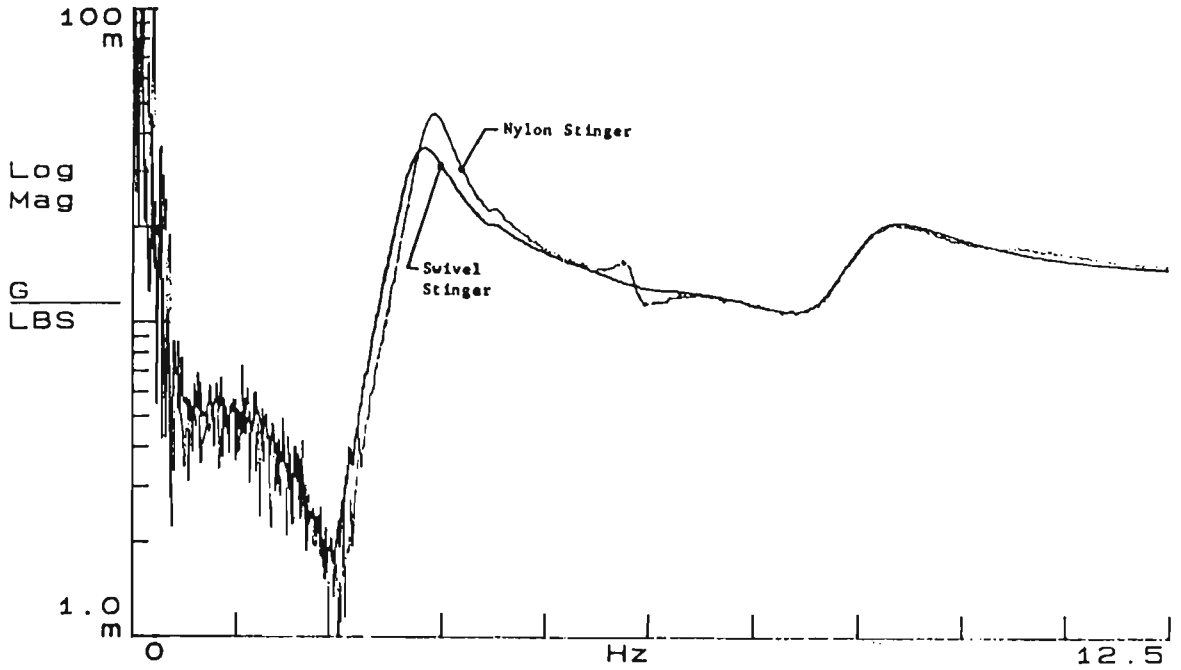

Figure 5 Nylon versus Swivel Stinger FRF

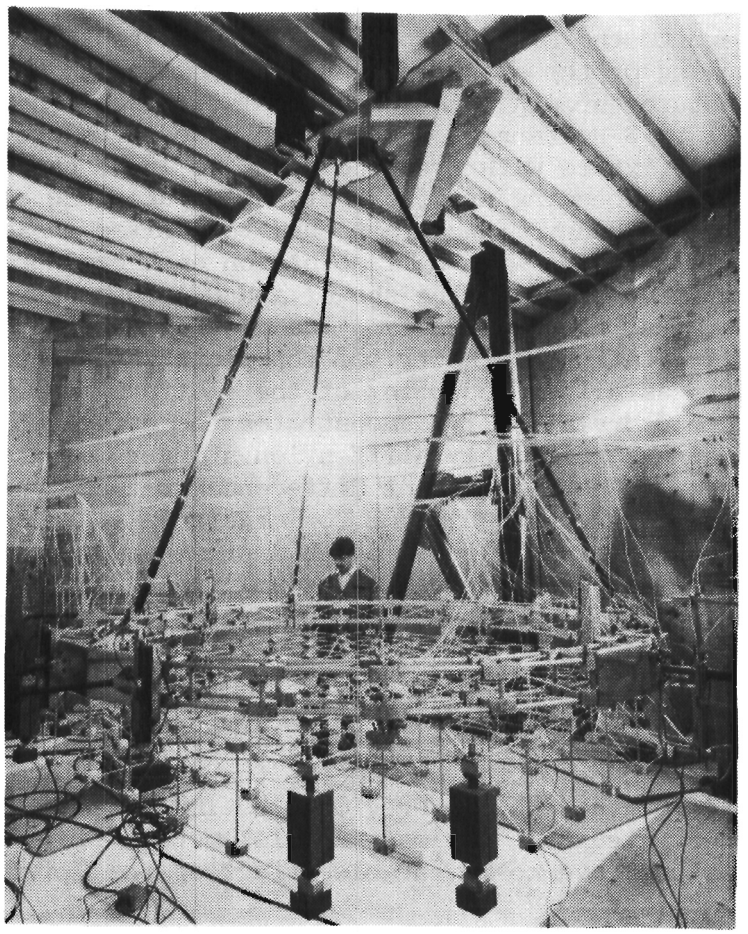

Figure 6 DTA Test Setup

Before acquisition of full 188 measurement data sets, several excitation methods were attempted at a few drive points to determine appropriate force levels and to identify the method which gave the highest quality data. Also, the necessary frequency resolution was determined by comparing curve fit results (multi-degree of freedom polynomial) from data collected for several values of resolution. The results indicated that a frequency resolution of 0.03125 Hz was adequate for acquiring the frequency response function (FRF) measurements in that fitting of data acquired at higher resolution produced virtually the same modal parameters as that acquired at 0.03125 Hz. Burst random excitation for 80% of the acquisition time period (32 seconds using 401 spectral lines and a 12.5 Hz bandwidth) with no windowing produced slightly better quality data than straight random excitation and Hanning windowing. Swept sine testing generated far better quality data but had little effect on curve fit results at points of relatively high response. To avoid conflicts in facility scheduling, multipoint random excitation and measurement techniques were selected for acquisition of the FRFs from which modal parameters would be extracted.

A Hewlett-Packard 3565 Modal System running Structural Measurement Systems (SMS) multi-input, multi-output software was used to acquire and process the measurements. This system, as configured for the DTA test, allows acquisition of up to 55 response points from up to four uncorrelated inputs. Thus, 220 FRF measurements may be acquired simultaneously. Using the acquisition parameters mentioned above, and taking ten averages, measurement of 55 response points takes only 5 minutes and 20 seconds. Including processing time, storage, and setup recall, a full set of 752 (188 x 4) FRF measurements took about 1.5 hours. This rapid data acquisition combined with the test chamber temperature stability allowed data to be acquired for the full DTA at a virtually constant temperature.

DATA ASSESSMENT AND ANALYSIS

Assessment and analysis of the measured data were conducted as the data sets were acquired. The FRF measurements were qualitatively reviewed immediately, and preliminary parameter identification was performed before the test configuration was changed. This process allowed discovery of several instrumentation problems and measurement anomalies which were investigated and corrected without repeating a configuration setup. Limitations of the available instrumentation resulted in poor measurements at points of low response, (typically on the order of 0.005 g's or less). This complicated the identification and separation of several closely spaced modes, particularly those involving coupled horizontal bending of the solar array masts and blankets. However, many modes were consistently identified and thus are likely to be very accurate. The following paragraphs discuss the FRFs and the process of parameter identification performed on the measurements.

Generally, the quality of the measurements was quite good at the drive points and at points of high response level. Figures 7(a) and 7(b) show typical drive point FRFs as examples of the data quality. The coherence for most of these measurements was excellent throughout the acquisition bandwidth. An anomaly seen in some of the data was high level noise in horizontal solar array blanket FRFs acquired using multipoint random excitation. Specifically, the response on the blanket due to excitation at points far removed from the solar array, such as the equipment platform, was very noisy as shown by Figure 8. This figure compares FRFs 20x/21x and 39y/21x. The level of 39y/21x is well above the noise floor of the PCB-302 accelerometers, and other data indicated that the level should have been much lower. Also, measurement 39y/42y, which was acquired simultaneously is much cleaner as shown by Figure 9.

The poor quality and high level of 39y/21x was probably caused by nonlinear behavior of the TMDs which contaminated the separation of responses performed by the multipoint random excitation algorithm which assumes a linear system. The TMD nonlinearity arises from the geometric lateral stiffening effect and plastic behavior of the TMD beams. In general, tests where the solar arrays were excited directly tended to produce somewhat more noisy measurements than when the arrays were not being driven directly, again probably due to nonlinear response of the TMDs.

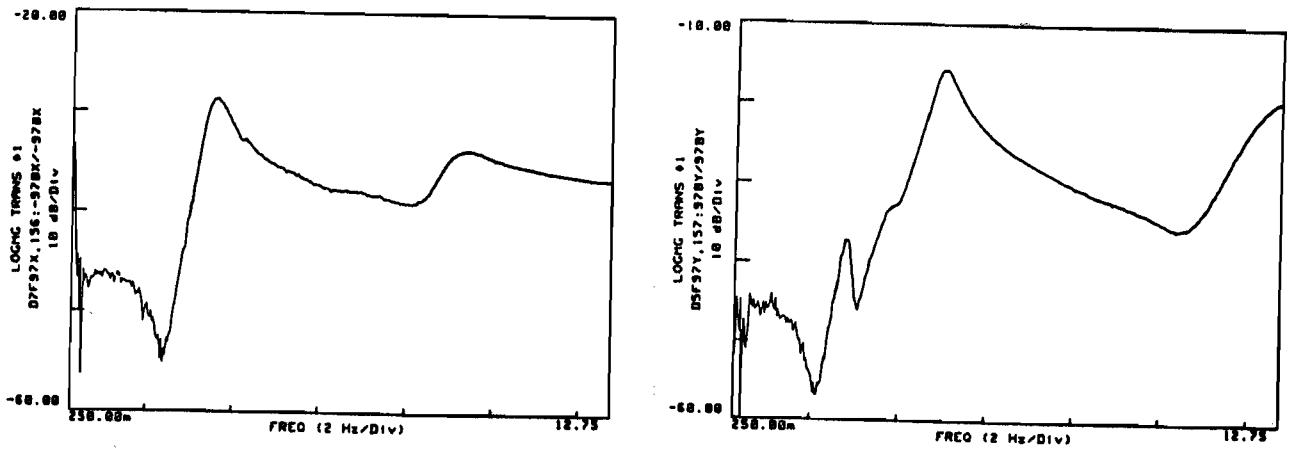

(a) 97x/97x (b) 97y/97

Figure 7 Typical Drive Point FRFs

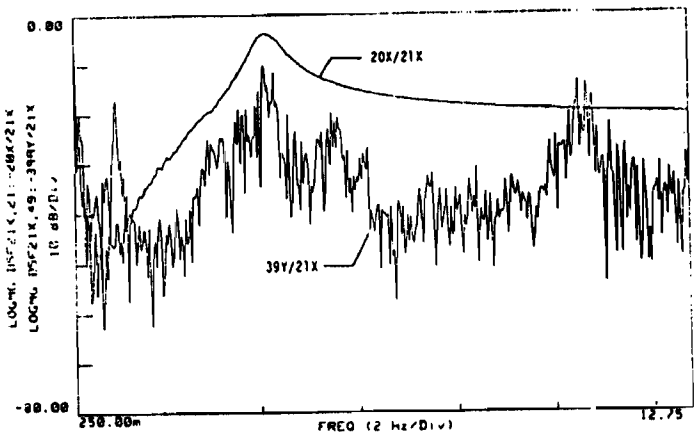

Figure 8 Measured FRFs: 39y/21x and 20x/21x

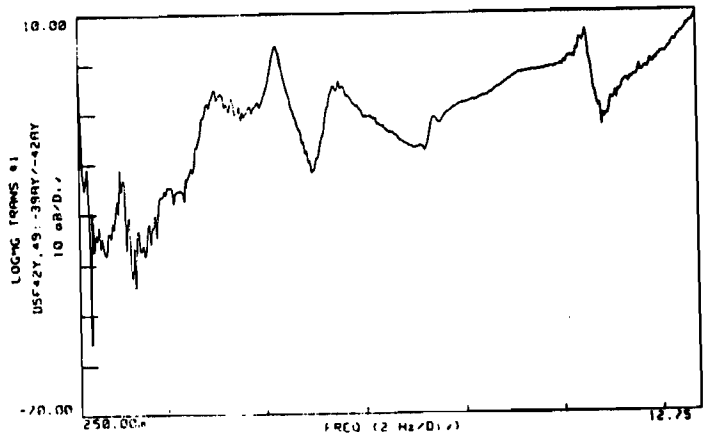

Figure 9 Measured FRF: 39y/42y

Parameter Identification

Identifying the number of modes and their parameters in the 1 to 10 Hz range of interest proved to be a challenging task. While several modes were easily and consistently fit, many closely spaced modes could not be adequately separated by local, multi-degree of freedom rational fraction polynomial (RFP) curve fitting techniques (Ref. 5). The combined effects of high modal density and high damping tended to mask distinct modes in the FRFs, thereby resulting in two or more modes being fit as a single mode. An example of this is seen by considering a portion of the measured FRF: 42y/42y.

As shown in Figure 10(a), a curve fit of the three modes apparent in the FRF from 2.44 to 6.47 Hz appears satisfactory and gives the modal parameters shown in the figure. However, when the three poles identified from 42y/42y are used to fit the measurement: 20x/42y, the extremely poor fit shown by Figure 10(b) results. This occurs because there are actually six modes present in the response at 42y. Note that 20x is on the axis of symmetry and thus should only show antisymmetric modes (refer to Figure 4). If 20x/42y is refit to determine the additional three modes as shown in Figure 10(c), and then all six of the identified poles are used to determine the modal residues for each FRF, satisfactory results are achieved for both measurements as shown by Figure 11. Attempting to determine all six poles from either measurement gives results like that shown in Figure 12 where the algorithm uses the additional modes to match

noise in the data. Essentially, the features in the FRF caused by the several modes are not as strong as noise in the measurement, even though the measurement is of acceptable quality. However, if the poles present in the FRF are known (and accurate), using the RFP method to find the residues results in a very good fit. This effect was seen even when working with extremely clean data.

Thus, the important task is to identify and estimate all the poles present in a given set of FRFs. Polyreference techniques were developed for just this purpose. The polyreference method tried on the DTA data was a time domain technique which tends to be sensitive to noise and did not work well on the highly damped DTA modes. Frequency domain polyreference techniques may work better on the DTA data, but this has not been investigated or demonstrated under the PACOSS program.

The aforementioned effects limited the accuracy of estimated modal damping ratios even when using the best measurements for determining a selected pole. While estimates of natural frequencies were consistent from one measurement to another, modal damping estimates varied by up to 20 percent for closely spaced, highly damped modes.

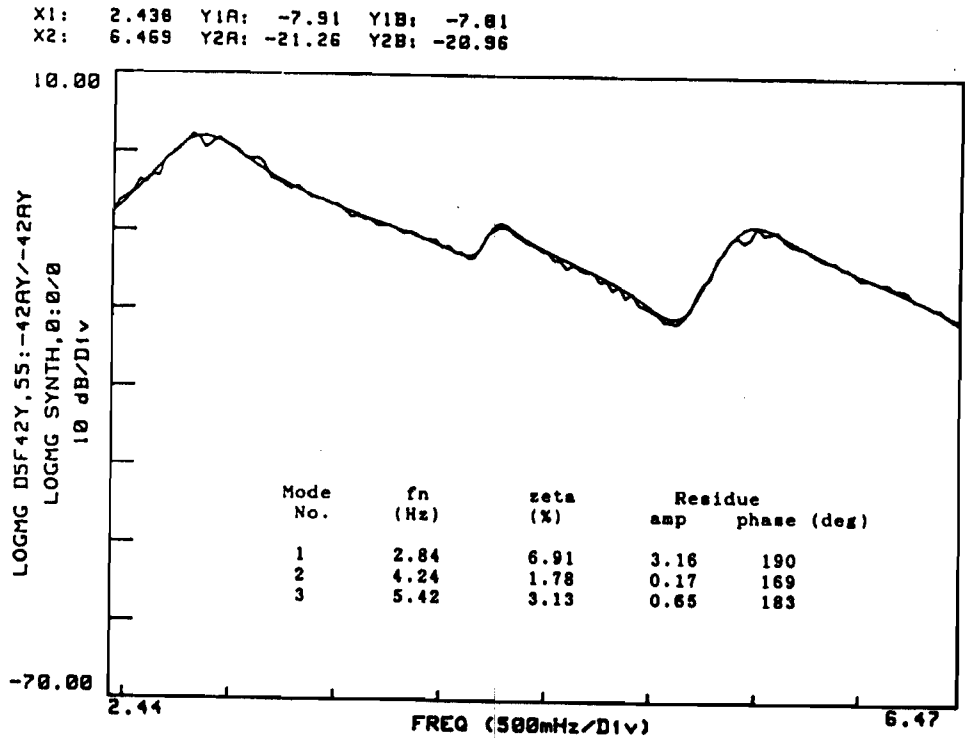

Figure 10(a) 3 Mode Fit of 42y/42y

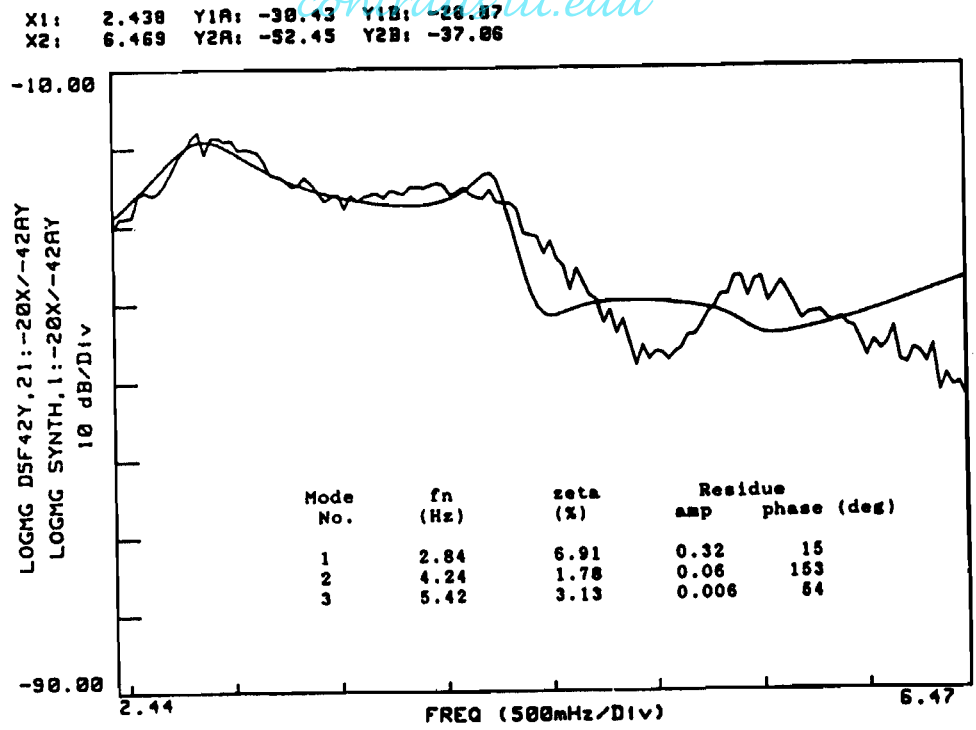

Figure 10(b) 3 Mode Fit of 20x/42y

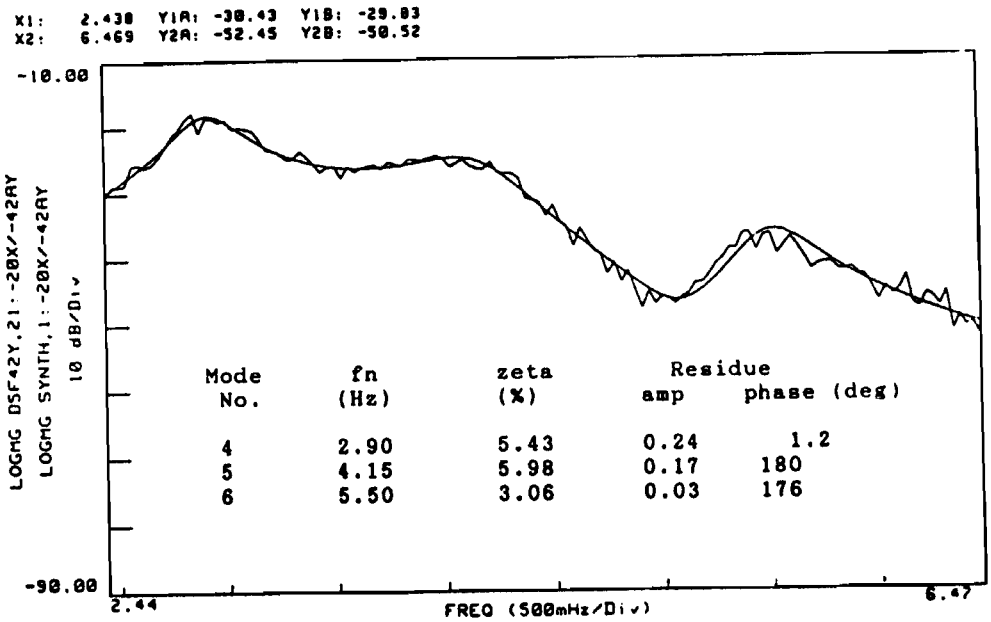

Figure 10(c) Second 3 Mode Fit of 20x/42y

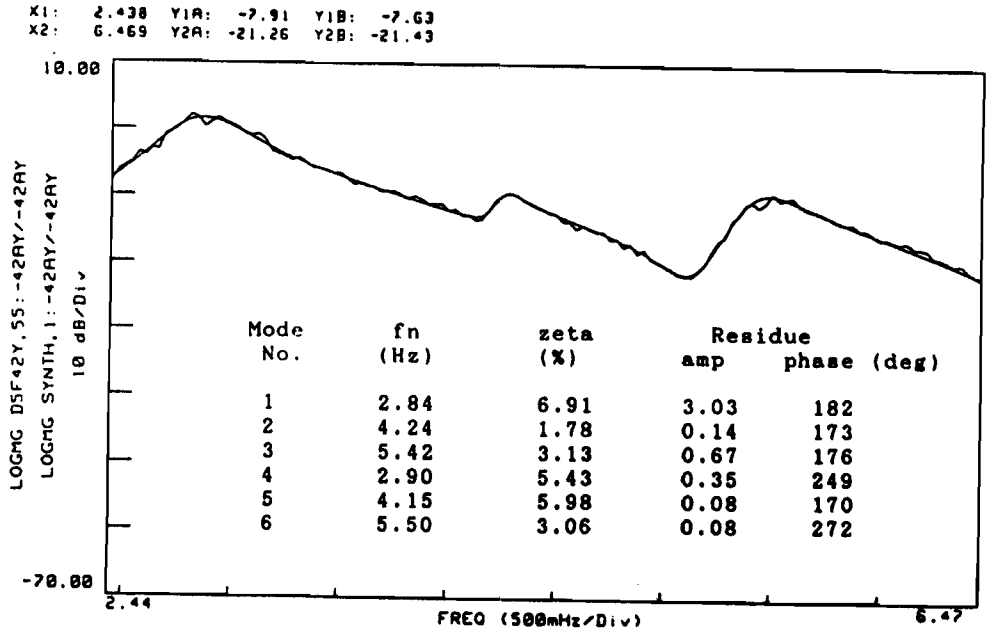

Figure 11 6 Mode Fit of 42y/42y

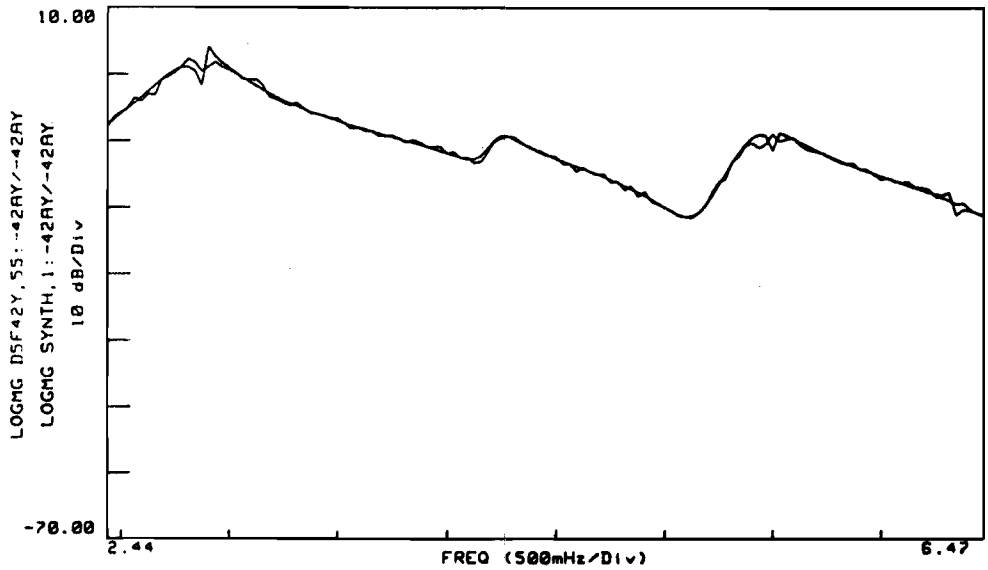

Figure 12 Local 6 Mode Fit of 42y/42y

A total of 22 unique modes were identified from the DTA testing. The identified modes are listed in Table 1 with the observed ranges listed for the modal frequencies and damping ratios. The quantity listed as weighted phase error in the table is defined by the following equation:

$$\overline{\theta} = \frac{\sum_{i=1}^{n\ dof} | \Delta\theta_i\ \phi_i |}{\sum_{i=1}^{n\ dof} | \phi_i |}$$

where:

$\overline{\theta}$ = weighted phase error

$\Delta\theta_i$ = phase difference (-90° to +90°) between dof i and dof of greatest magnitude

ϕ_i = modal magnitude at dof i

Weighted phase error is an indication of the quality of the synthesized mode shape. Generally, the smaller the weighted phase error, the more accurate the estimate of the mode shape. Note that in Table 1, relatively high phase error generally corresponds to modes exhibiting greater scatter in their frequency and damping estimates. The high phase error is attributable to a failure of the curve fitting technique to fully separate closely spaced, highly damped modes. This occurs when the response components present in an FRF due to individual modes (complex residues) are not correctly determined by the particular parameter identification technique applied to the data.

The procedure used in determining estimates of the mode shapes was to obtain the best estimates of the poles in a given data set and frequency range. The poles were obtained using the RFP multi-degree of freedom method. Once a satisfactory and complete set of poles was obtained, the mode shapes were found by holding the poles constant while determining the residues for each measurement. Based on the consistency of results, and on orthogonality products discussed below, a set of orthogonal modes was selected as the "best" measured modes for use in correlation with the analytic model.

Table 1 Summary of Identified Modes

Measured Mode No.	Description	Range of f_n (Hz)	Range of ζ (%)	Range of Weighted Phase Error (Degrees)	Fit Confidence*
1	1st Blanket Bending, Solar Array 1	1.02 - 1.04	3.0 - 4.1	19.9 - 33.6	M
2	1st Blanket Bending, Solar Array 2	1.10 - 1.11	4.8 - 6.0	20.7 - 24.7	M
3	1st Symetric Ring Truss Bending	2.59 - 2.61	2.4 - 4.7	8.1 - 15.2	H
4	Symmetric Horizontal Solar Array Mast Bending	2.80 - 2.85	3.4 - 7.0	16.9 - 42.4	L
5	Anti-Symmetric Horizontal Solar Array Mast Bending	2.87 - 2.94	4.4 - 9.6	28.3 - 41.0	L
6	Anti-Symmetric Solar Array Vertical Bending w/Box Truss Rocking	3.25 - 3.30	4.9 - 6.3	19.4 - 30.9	H
7	Anti-Symmetric Solar Array Vertical Bending w/Tripod	3.53 - 3.66	5.9 - 8.8	15.1 - 26.9	H/M
8	Equip Platform Vertical Bending w/Tripod & Solar Array Symmetric Bending	3.72 - 3.88	4.3 - 5.7	11.2 - 30.3	H
9	Equip Platform Horizontal Bending	4.10 - 4.13	7.1 - 7.2	19.4 - 20.0	H
10	1st Blanket Torsion, Solar Array 1	4.10 - 4.30	1.6 - 2.2	9.0 - 16.0	H
11	1st Blanket Torsion, Solar Array 2	4.18 - 4.33	1.1 - 2.6	8.0 - 26.2	H
12	Symmetric Antenna Bending w/Tripod Bending	4.83 - 4.96	4.5 - 5.8	5.6 - 21.3	H/M
13	Tripod Torsion	4.95 - 4.98	5.5 - 6.0	13.9 - 20.8	H/M
14	Symmetric Antenna Dish, Equipment Platform, Tripod	5.04 - 5.45	4.6 - 13.4	19.0 - 42.6	M/L
15	2nd Blanket Bending, Solar Array 2	5.41 - 5.47	2.9 - 3.8	6.4 - 18.9	H
16	2nd Blanket Bending, Solar Array 1	5.34 - 5.48	2.5 - 3.0	10.0 - 23.7	H
17	Anti-Symmetric Tripod Bending w/Box Rocking & Solar Array Vertical Bending	6.37 - 6.48	7.8 - 12.7	20.5 - 43.0	L
18	2nd Blanket Torsion, Solar Array 1	8.89	5.5	21.1	M
19	Anti-Symmetric Tripod Bending	8.77 - 9.04	3.5 - 7.0	17.6 - 28.3	L
20	Symmetric Tripod Bending w/Antenna & Ring Bending	9.10 - 9.26	6.9 - 8.6	24.6 - 29.6	L
21	2nd Blanket Torsion, Solar Array 2	9.32	4.5	16.5	M
22	Symmetric Antenna Dish Bending	9.17 - 9.47	5.4 - 10.3	13.5 - 27.7	M

* L = Low
M = Moderate
H = High

ANALYTIC MODEL CORRELATION

The measured results agreed fairly well with the pretest analytic model. This indicated that data from a sufficient number of excitation points had been acquired to allow identification of all major flexible modes below 10 Hz. The following paragraphs discuss the post-test tuning of the DTA finite element model and present the final comparison of predicted and measured modal parameters.

A comparison of the predicted and measured natural frequencies and mode shapes indicated that the dynamic coupling of the solar arrays to the rest of the DTA was different from that predicted by analysis. Final correlation and tuning of the solar array substructure model with the results from substructure testing had not been completed before the full DTA test. Therefore, modification of the DTA solar array models involved completing the substructure tuning.

Results from the solar array substructure modal surveys indicated that the initial modeling of the root assembly was too stiff. This was due to the physical nature of the actual root assembly which consists of a solid aluminum insert bonded inside the solar array mast. In order to more accurately characterize the stiffness of the bonded root assembly, a model including the inner member, the mast tubing, and the bonding material was constructed for comparison with the properties of the original model. The inner member was modeled using solid elements, as was the bonding material, and the mast tubing was modeled using plate elements. In the analyses, the stiffnesses of the various members alone were adjusted to have equivalent stiffnesses to beams. For example, unit loads were applied to the insert model alone and the material properties adjusted so that the resulting deflections and rotations were the same as those of a beam with a solid section of the same size.

The stiffness of the bonded assembly model was 62% that of an equivalent beam. It was noted, however, that the model might be in error due to the use of solid elements. To determine the accuracy of the model, the bonding material was replaced with aluminum and the resulting stiffness was again compared with an equivalent beam. This analysis showed that the model using aluminum properties for the bonding material was 80% as stiff as an equivalent beam. Therefore, the final stiffness of the assembly was adjusted to be 0.62/0.8 or 78% that of a uniform aluminum beam.

The pretest DTA model also did not include the deformed geometry of the solar arrays. The tip of the solar array mast deflected more than 5 inches under gravity over a mast length of 8 feet. This geometry was included in the final DTA analysis.

The only other significant change in the DTA modeling was the addition of differential stiffness in the tripod analysis to account for compression in the tripod legs. A minor correction made to the modeling was the deletion of some accelerometer masses that had remained in the substructure models from correlation with substructure modal survey results. These small masses were not deleted from the pretest DTA model in the interest of expediency in completing the pretest analysis. Note that no arbitrary changes such as stiffness or mass adjustments were made in order to obtain better agreement between the analysis and test results. This philosophy, followed throughout the development of the substructure models, has resulted in a DTA model which is based solely on standard and measured physical properties. In fact, the final DTA model could be considered a rigorous pretest model.

In order to more accurately represent the frequency dependency of VEM material properties, the component models were run with both 4 Hz and 9 Hz VEM stiffness. Modes below 6.5 Hz were taken from the 4 Hz run, and those above from the 9 Hz run. VEM loss factors at specific modal frequencies were used in the damping calculations.

Results Comparison

Analysis of the tuned DTA model was performed using direct stiffness coupling of the reduced substructure models. Analytic modal damping ratios were determined via the modal strain energy (MSE) method using the appropriate loss factors (Ref 6).

For discussion of the experimentally identified modes, the analytic modes may be grouped into four categories based on the modal strain energy distributions. The four categories and number of flexible modes in each category are:

10	Global modes
10	Nearly repeated solar array blanket modes (symmetric/antisymmetric pairs)
7	Local appendage modes
12	Tuned mass damper (TMD) modes

Global modes are defined as modes in which no one component possesses more than 90 percent of the modal strain energy. These modes are typically of greatest interest to the analyst because of their importance to system performance. They are the modes most easily disturbed by spacecraft maneuvers and, by their nature, affect the entire system. Therefore, accurate prediction of global modes and the associated damping design (passive or active) for those modes is critical to achieving system performance goals.

The five pairs of nearly repeated solar array blanket modes posed a problem in terms of correlation with experimental modes through a cross orthogonality product. Experimentally, the synthesized modes tended to result in either one blanket or the other possessing all the motion, i.e., they looked like a linear combination of the analytic pair. For repeated roots, any linear combination of the repeated mode shapes is itself a mode shape or, eigenvector. Thus, the analytic blanket mode pairs were added and subtracted to obtain modes for comparison with the measured modes. Two pairs of repeated modes are dominated by the TMDs. The high damping and somewhat local nature of these four modes precluded their identification.

The local appendage modes include a variety of modes where a single substructure possesses more than 90 percent of the modal strain energy. One of the predicted appendage modes was not identified because it involved only antenna dish bending which could not be adequately excited without driving the dish directly.

The 12 TMD modes are very local in nature. They are uncoupled from the rest of the DTA and may only be disturbed by directly exciting the TMDs. Since any attachment of a stinger to a TMD would drastically alter its behavior, no attempt was made to identify these modes.

The points discussed above led to a set of 22 target modes. During analysis of the test data, it became obvious that the nonlinear behavior of the TMDs, and the relatively high noise level of the TMD instrumentation had seriously degraded the measurements on the TMDs. This degradation was serious enough to introduce large errors into the synthesized TMD modal deflections. Therefore, orthogonality products were computed without the TMD measurements.

In order to perform the orthogonality checks without the TMD measurements, a mass matrix reduced to the measurements to be used in the orthogonality products had to be generated. A static reduction of the DTA mass and stiffness matrices without including the TMD measurements results in significant error in the solar array blanket modes. Therefore, this method could not be used to generate a reduced mass matrix. An alternate approach to generating a reduced mass matrix is to use the analytic modes calculated from a valid reduction. Briefly, the unmeasured degrees of freedom are deleted from the modal vectors and the resulting modes are then used to compute the test analysis matrix (TAM) using the pseudo-inverse:

$$TAM = (\phi^T)^{-\ddagger} \cdot \phi^{-\ddagger}$$

where

$\phi^{-\ddagger}$ is the pseudo-inverse: $(\phi^T\phi)^{-1}\,\phi^T$

Conditioning problems will arise if the modal vectors are very similar (nearly linearly dependent). This can occur if the primary degrees of freedom involved in a mode are deleted but the mode is retained in generating the test analysis mass matrix. For the DTA, only the target modes were retained, and all TMD measurements were deleted.

As previously mentioned, measured modal damping ratios tended to exhibit some variation depending on the identification method. However, the modes selected for comparison with the analytic results were chosen on the basis of small weighted phase error and good orthogonality. Therefore, the damping ratios of the selected modes were assumed to be the best estimates of the true DTA behavior, and were the specific values used for comparison with the analytic results. The results are presented in Table 2 which lists the comparison of the measured and analytically predicted frequencies and damping ratios of the target modes. Also listed in the table are the diagonal terms of the unnormalized generalized mass and cross orthogonality products. These products were computed using the real measured modes defined as:

$$\phi_{i_{real}} = \phi_i \cos \theta_i$$

where:

$\phi_{i_{real}}$ = real modal amplitude at DOF i

ϕ_i = complex modal amplitude at DOF i

θ_i = phase angle between DOF i and DOF of greatest magnitude

The orthogonality products are defined as:

$$GM = \phi^T_{real} \cdot TAM \cdot \phi_{real}$$

where:

ϕ_{real} = the measured real mode shape as given above

TAM = is mass matrix as given in Section 4.3

Note that the modal synthesis technique used in computing the mode shapes should produce modes with unity generalized mass.

$$XORTH = \overline{\phi}^T_{real} \, TAM \, \phi_a$$

where:

$\overline{\phi}_{real}$ = ϕ_{real} normalized to TAM

ϕ_a = the analytic modes matrix used to generate TAM

The data presented in Table 2 show that all the target modes were identified and that most correlate very well with the analytic predictions. Correspondence of frequencies is excellent with the exception on modes 9 and 18. Mode 9 is a local equipment platform mode and mode 18 is a local antenna mode which is sensitive to the postbuckled state of the antenna dish. The postbuckled state and effects were noted during the antenna substructure modal survey, but could not be accurately modeled.

Damping estimates agree reasonably well with the predicted values. In fact, the analytic value is bracketed by the measured range in many cases (see Table 1). Excellent qualitative agreement of the modes is shown in Figures 13(a) and (b) which present plots of the corresponding measured and predicted shapes for two global modes.

While the diagonal cross-orthogonality terms listed in Table 2 and the mode shape plots indicate good correlation for most of the modes, the full orthogonality products exhibit significant off diagonal coupling. The self orthogonality normalized to unity generalized mass is given in Table 3, and the cross orthogonality with the analytic target modes is given in Table 4.

Table 2 Comparison of Identified and Predicted Modal Parameters

Target Mode No.	Analytic f_n (Hz)	Analytic ζ (%)	Measured Mode No.	Measured Results * f_n (Hz)	Measured Results * ζ (%)	Orthogonality Results GM	Orthogonality Results X-Orth Diagonal Term
1	1.00	4.2	1	1.03	4.1	0.83	0.96
2	1.03	4.2	2	1.10	6.0	0.71	0.99
3	2.61	2.8	3	2.61	3.6	1.06	0.97
4	3.01	5.0	4	2.81	4.4	2.70	0.64
5	3.08	4.0	5	2.89	7.0	3.02	0.68
6	3.29	4.4	6	3.25	5.0	0.94	0.93
7	3.50	8.2	7	3.53	8.8	1.27	0.88
8	3.70	4.7	8	3.72	5.2	1.01	0.97
9	3.81	4.0	9	4.13	7.1	0.90	0.99
10	4.14	2.0	10	4.15	1.6	0.87	0.91
11	4.14	2.0	11	4.24	1.6	1.03	0.91
12	4.60	7.8	12	4.83	4.5	3.12	0.88
13	4.81	10.4	14	5.04	11.4	0.85	0.94
14	4.86	7.0	13	4.96	5.5	1.96	0.97
15	5.32	4.0	15	5.41	3.8	0.83	0.98
16	5.32	4.0	16	5.43	3.0	0.74	0.95
17	6.12	10.0	17	6.48	12.7	1.43	0.91
18	7.52	6.0	22	9.40	10.3	0.98	0.76
19	8.94	1.8	18	8.90	5.5	0.67	0.96
20	8.95	1.8	21	9.32	4.5	0.57	0.98
21	9.04	6.8	19	8.92	7.0	1.11	0.96
22	9.28	7.0	20	9.26	8.6	2.26	0.88

* See Table 1 for Variation in Results.

Table 3 Normalized Generalized Mass Matrix

NORMGM

fn :	1.03	1.10	2.61	2.81	2.89	3.25	3.53	3.72	4.13	4.15	4.24	4.83	4.96	5.04	5.42	5.43	6.48	8.89	8.92	9.26	9.32	9.40
ROW	1	2	3	4	5	6	7	8	9	10	11	12	13	14	15	16	17	18	19	20	21	22
1	1.00	0.12	-0.11	0.57	-0.10	-0.12	-	-	-	-0.19	-	-	-	-	-	-	-	0.14	-	-	-	-
2	0.12	1.00	-	0.52	0.65	-	-	-	-	-	-0.25	-	-	-	-	-	-	-	-	-	-	-
3	-0.11	-	1.00	-0.31	-	-	-	0.12	-	-	-	-	-	-	-	-	-	-	-	-	-	-
4	0.57	0.52	-0.31	1.00	0.26	-	-	-	-	-0.17	-0.20	-	-	-	-	-	-	0.10	-	-	-	-
5	-0.10	0.65	-	0.26	1.00	-	-	-	-	-	-0.23	-	-	-	-	-	-	-	-	-	-	-
6	-0.12	-	-	-	-	1.00	-	-	-	0.11	-	-	-	-	-	-	-	-	-	-	-	-
7	-	-	-	-	-	-	1.00	-	-	-	-	-	-	-	-	-	-	-	0.23	-0.16	-	-
8	-	-	0.12	-	-	-	-	1.00	-	-	-	-	-	-	-	-	-	-	-	0.14	-	-
9	-	-	-	-	-	-	-	-	1.00	-	-	-	-	-	-	-	-	-	-	-	-	-
10	-0.19	-	-	-0.17	-	0.11	-	-	-	1.00	-	-	-	-	-	-	-	-	-	-	-	-
11	-	-0.25	-	-0.20	-0.23	-	-	-	-	-	1.00	-	-	-	-	-	-	-	-	-	-	-
12	-	-	-	-	-	-	-	-	-	-	-	1.00	-0.15	0.31	-	-	-0.15	-	-	-	-	0.36
13	-	-	-	-	-	-	-	-	-	-	-	-0.15	1.00	0.11	-	-	0.14	-	0.15	0.22	-	-
14	-	-	-	-	-	-	-	-	-	-	-	0.31	0.11	1.00	-	-0.15	-	-	-	0.31	-	0.35
15	-	-	-	-	-	-	-	-	-	-	-	-	-	-	1.00	-	-	-	-	-	-	-
16	-	-	-	-	-	-	-	-	-	-	-	-	-	-0.15	-	1.00	-0.11	-	-	-	-	-
17	-	-	-	-	-	-	-	-	-	-	-	-0.15	0.14	-	-	-0.11	1.00	-	0.45	-0.12	-	-0.11
18	0.14	-	-	0.10	-	-	-	-	-	-	-	-	-	-	-	-	-	1.00	-	-	-	-
19	-	-	-	-	-	-	0.23	-	-	-	-	-	0.15	-	-	-	0.45	-	1.00	-0.16	-	-
20	-	-	-	-	-	-	-0.16	0.14	-	-	-	-	0.22	0.31	-	-	-0.12	-	-0.16	1.00	-	0.18
21	-	-	-	-	-	-	-	-	-	-	-	-	-	-	-	-	-	-	-	-	1.00	-
22	-	-	-	-	-	-	-	-	-	-	-	0.36	-	0.35	-	-	-0.11	-	-	0.18	-	1.00

Table 4 Cross-Orthogonality Product

"CROSS-ORTHOGONALITY CHECK (EXPERIMENTAL/ANALYTICAL)"

fno :		1.00	1.03	2.61	3.01	3.08	3.29	3.50	3.70	3.81	4.14	4.15	4.60	4.81	4.86	5.32	5.32	6.12	7.52	8.94	8.95	9.04	9.28
fn	ROW	1	2	3	4	5	6	7	8	9	10	11	12	13	14	15	16	17	18	19	20	21	22
1.03	1	0.96	0.21	-	-	-	-	-	-	-	0.11	-	-	-	-	-	-	-	-	-	-	-	-
1.10	2	-	0.99	-	-	-	-	-	-	-	-	-	-	-	-	-	-	-	-	-	-	-	-
2.61	3	-0.14	-	0.97	-	-	-	-	-	-	-	-	-	-	-	-	-	-	-	-	-	-	-
2.81	4	0.46	0.55	-0.14	0.64	-0.11	-	-	-	-	-0.16	-	-	-	-	-	-	-	-	-	-	-	-
2.89	5	-0.23	-0.63	-	0.13	0.68	-	-	-	-	0.10	-0.10	-	-	-	-	-	-	-	-	-	-	-
3.25	6	-0.11	-	-	-	-	0.93	0.30	-	-	-	-	-	-	-	-	-	-	-	-	-	-	-
3.53	7	-	-	-	-	-	-0.35	0.88	-	-	-	-	-	-	-	-	-	-	-	-	-	0.20	-0.14
3.72	8	-0.10	-	-	-	-	-	-	-0.97	-	-	-	-	-	-	-	-	-	-	-	-	-	-
4.13	9	-	-	-	-	-	-	-	-	0.99	-	-	-	-	-	-	-	-	-	-	-	-	-
4.15	10	-0.30	-	-	0.15	-0.17	-	-	-	0.12	0.91	-	-	-	-	-	-	-	-	-	-	-	-
4.24	11	-	-0.32	-	-	0.10	-	-	-	-	-	0.93	-	-	-	-	-	-	-	-	-	-	-
4.83	12	-	-	-	-	-	-	-	-	-	-	-	-0.88	0.37	-	-	-	-	-0.29	-	-	-	-
4.96	13	-	-	-	-	-	-	-	-	-	-	-	0.14	-	0.97	-	-	-	-	-	-	-	0.12
5.04	14	-	-	-	-	-	-	-	-	-	-	-	-	0.94	-	-0.10	-0.20	-	-	-	-	-	0.10
5.42	15	-	-	-	-	-	-	-	-	-	-	-	-	-	-	0.98	-	-	-	-	-0.16	-	-
5.43	16	0.11	-	-	-	-	-	-	-	-	-0.10	-	-	-	-	-	0.95	-	-	-0.24	-	-	-
6.48	17	-	-	-	-	-	-	-	-	-	-	-	0.15	-	-	-	-	0.91	-	-	-	0.28	-
8.89	18	0.13	-	-	-	-	-	-	-	-	-	-	-	-	-	-	-0.18	-	-	-0.96	-	-	-
8.92	19	-	-	-	-	-	-	-	-	-	-	-	-	-	-	-	-	0.17	-	-	-	0.97	-
9.26	20	-	-	-	-	-	-	-	-0.10	-	-	-	-	0.25	0.10	-	-	-	0.30	-	-	-0.13	0.88
9.32	21	-	-	-	-	-	-	-	-	-	-	-	-	-	-	-0.15	-	-	-	-	-0.99	-	-
9.40	22	-	-	-	-	-	-	-	-	-	-	-	-0.49	0.36	-	-	-	-	0.76	-	-	-	-0.18

-: Absolute Value Less Than 0.10

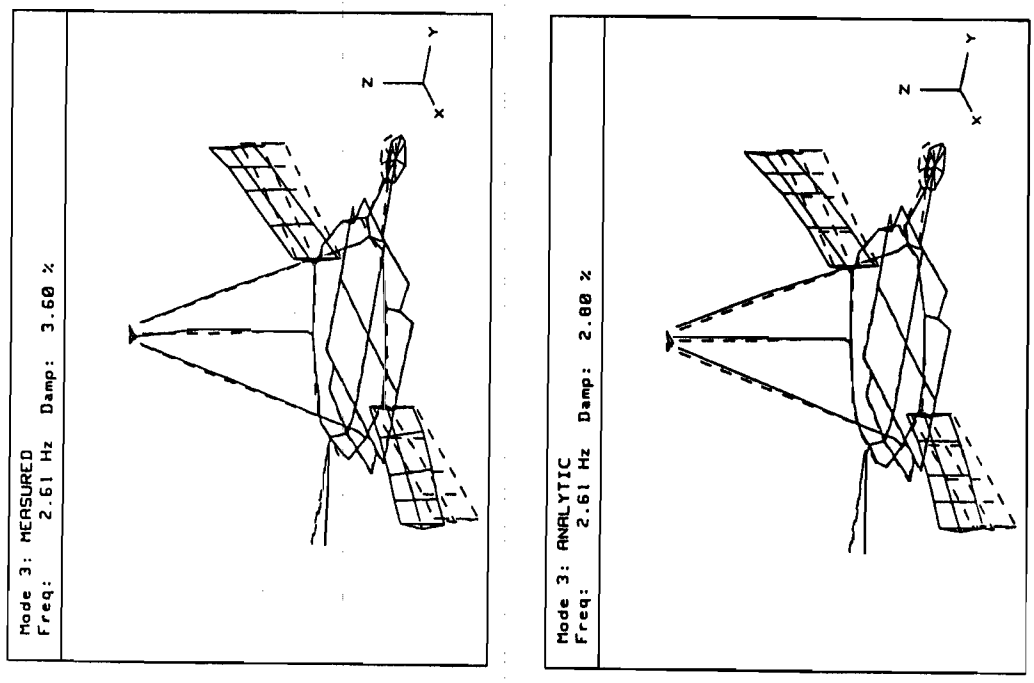

Figure 13(a) Measured Mode 3 and Analytic Mode 3

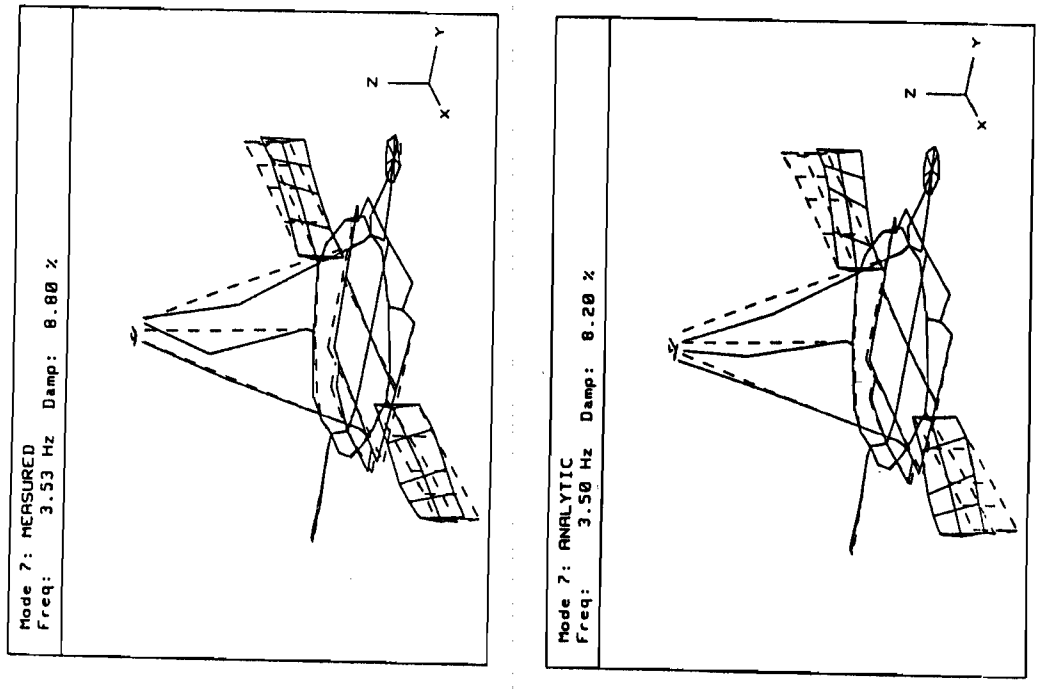

Figure 13(b) Measured Mode 7 and Analytic Mode 7

The correlation between the measured and analytically predicted modes is exceptional considering the dynamic complexity of the DTA. All global modes were predicted accurately in terms of frequency and damping. However, the orthogonality products show significant coupling between similar modes. Consideration of both the generalized mass and cross orthogonality products gives an indication of the source of error. Some experimentally synthesized modes appear to be quite accurate while others possess error due to the identification difficulties previously discussed.

For example, experimental modes 6 and 7 (see Table 2) exhibit little coupling in the self orthogonality product, (Table 3). However, there is significant coupling on the order of 30% with their analytic counterparts as shown by Table 4. Together, these observations indicate that these two particular experimental modes are accurate estimates of the true behavior of the DTA. Other factors such as repeatability and small phase error also indicate that the 3.25 Hz and 3.53 Hz modes were accurately identified. Thus, the coupling of terms corresponding to these modes in the cross orthogonality product is attributable to some physical difference between the actual DTA and the finite element model. Comparison of a measured FRF with the corresponding analytic prediction (Figure 14) confirms that the structure behaves somewhat differently in the 3 to 4 Hz range due to these modes. Note that modes 6 and 7 are both antisymmetric, global modes which are rather closely spaced in terms of frequency considering the damping present. Modes such as these can be quite sensitive to small variations in the structure and thus are difficult to precisely predict.

Examples of modes not accurately identified are measured modes 4 and 5. The presence of nearby, highly damped TMD / blanket modes, and noisy TMD measurements, made consistent parameter estimation of these modes impossible using the RFP technique previously mentioned. This is indicated by the variation shown in Table 1. Thus, the relatively poor orthogonality results for these two modes are primarily due to error in the measured mode shapes. However, as shown in Figure 15, comparison of analytic and measured FRFs indicates that while the behavior is similar, there is a definite frequency difference between the analytic model and actual DTA in the 2 to 3 Hz range. This must be due to a modeling error.

Overall, the agreement between measured and predicted DTA modal parameters is excellent. This is shown by agreement of modal frequencies and damping ratios, and demonstrated by comparison of measured and predicted FRFs. Coupling in the orthogonality products is primarily due to parameter identification difficulties traceable to the algorithms used on the measured data. Use of more sophisticated techniques may improve the synthesized mode shapes and thereby the orthogonality products.

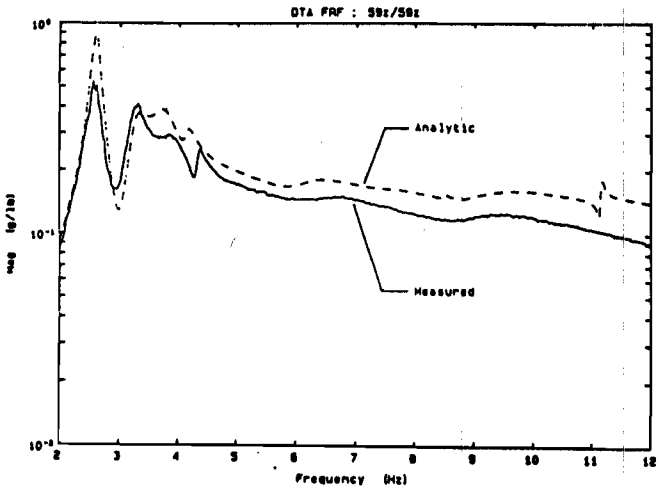

Figure 14 Measured and Analytic FRFs: 59z/59z

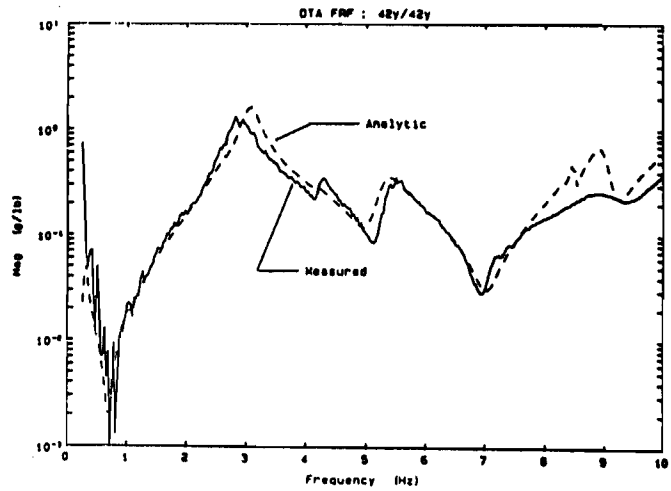

Figure 15 Measured and Analytic FRFs: 42z/42z

CONTROL SYSTEM PERFORMANCE

Investigation of the DTA active damping system performance was conducted by performing the same tests as in open-loop cases but with the control system on, and feedback gains set to design values. Analysis of the local velocity feedback system was accomplished by coupling the actuator dynamics and feedback gains to the DTA modal model. The active damping system consisted of six proof mass actuators mounted on the DTA ring truss at the locations shown in Figure 16. These locations were selected in order to actively damp the 2.6 Hz DTA mode. Figure 17 shows a photo of two actuators attached to the ring truss. The control law applied to the DTA was local direct velocity feedback where the inertial velocity at a control point is fed back to apply a proportional force opposite the velocity. Ideally, this force appears as a dashpot to ground on the structure. Feedback gain settings were selected such that the active control system would apply 5% modal damping to the 2.6 Hz mode (in addition to the passive damping present). Besides the inertial velocity feedback, relative velocity between the proof mass and housing was sensed and fed back in order to adjust the local damping of the actuator second order system.

Table 5 lists the actual feedback settings used in the closed-loop tests. Analysis predicted that the control system would apply significant damping to four modes in the 1 to 10 Hz range. Fitting of the data from the tests confirmed the increased damping in four modes with all other modes not significantly affected.

The design feedback levels and actuator dynamics were coupled to the tuned DTA modes in order to predict the closed-loop damping. Table 6 lists the predicted closed-loop damping ratios together with the corresponding range of measured values for the four actively controlled modes. Again, variation in the damping estimates was seen depending on fit method. The data demonstrate that the control system, while functioning as expected, had somewhat less authority in the 2.6 Hz mode than predicted. This was due to a somewhat smaller modal amplitude at the control points than predicted.

Comparison of predicted to measured FRFs at the control points showed good qualitative agreement and verified that the control system was behaving as predicted. Figure 18 presents the measured and predicted FRFs at control point 3. Note the very low levels of the transfer functions which, in the modal survey test, resulted in RMS accelerations on the order of 0.005 g's. Even with these low acceleration levels, the control system performed well, indicating that friction in the actuators was not a factor in the testing. At points of higher response such as the solar array tip, the desired effect of actively lowering the response of the 2.6 Hz mode was achieved. This is shown by Figures 19 and 20 which present the open- and closed-loop FRF and decay trace respectively, at the solar array tip.

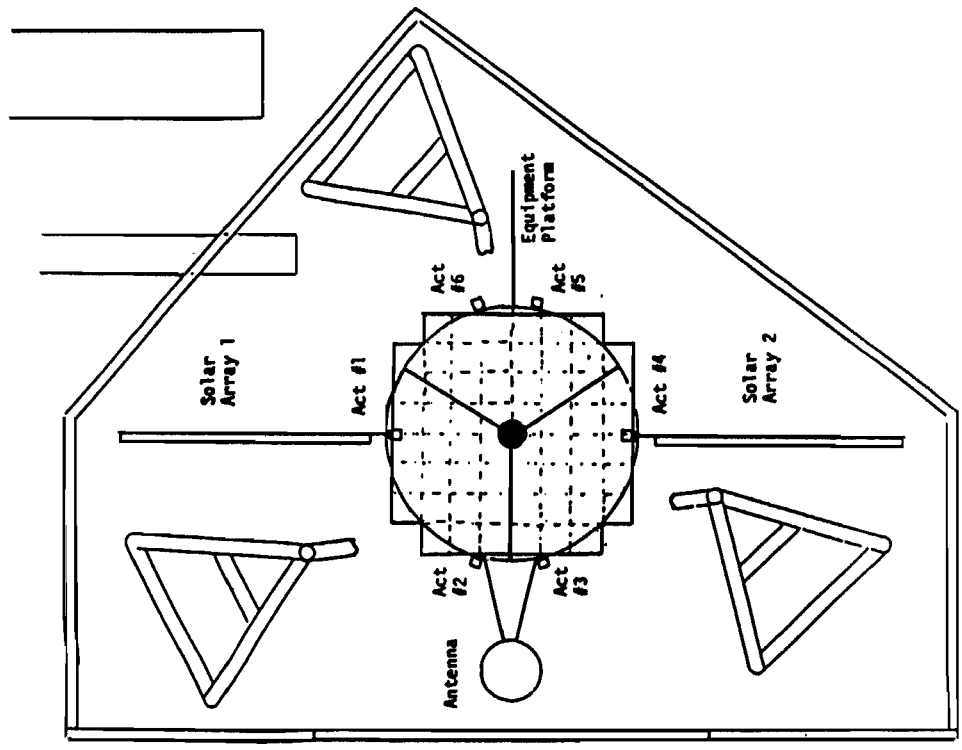

Figure 16 DTA Actuator Locations

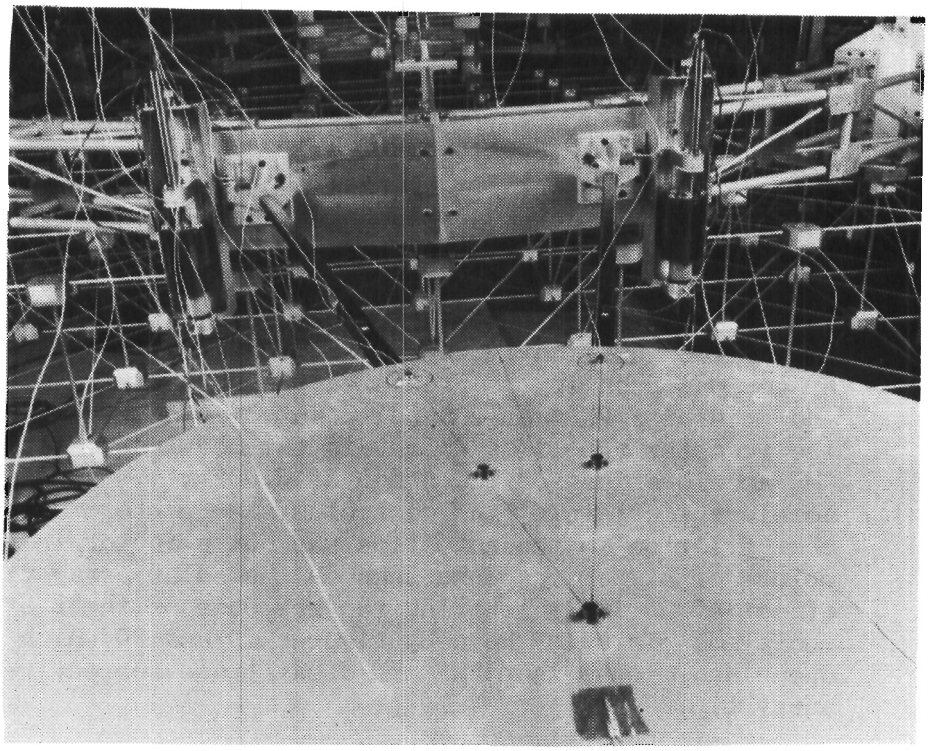

Figure 17 Actuators Mounted on DTA

Table 5 Feedback Gain Settings

RELATIVE VELOCITY FEEDBACK SETTINGS		INERTIAL VELOCITY FEEDBACK SETTINGS	
(%)	(ζ_a %)	(%)	(lb-sec/in.)
50	38	89	4.6
22	20	65	3.5
25	20	74	3.5
50	38	84	4.6
25	20	70	3.5
27	20	69	3.5

Table 6 Closed-Loop Results

TARGET MODE NO.	f_n (Hz)		ζ (%)	
	ANALYTIC	MEASURED RANGE	ANALYTIC	MEASURED RANGE
3	2.54	2.51 → 2.60	8.1	6.7 → 8.1
13	4.67	4.91 → 5.05	15.7	13.0 → 16.0
17	5.96	6.35 → 6.40	17.8	15.1 → 19.6
22	9.20	8.94 → 9.38	11.7	12.8 → 13.1

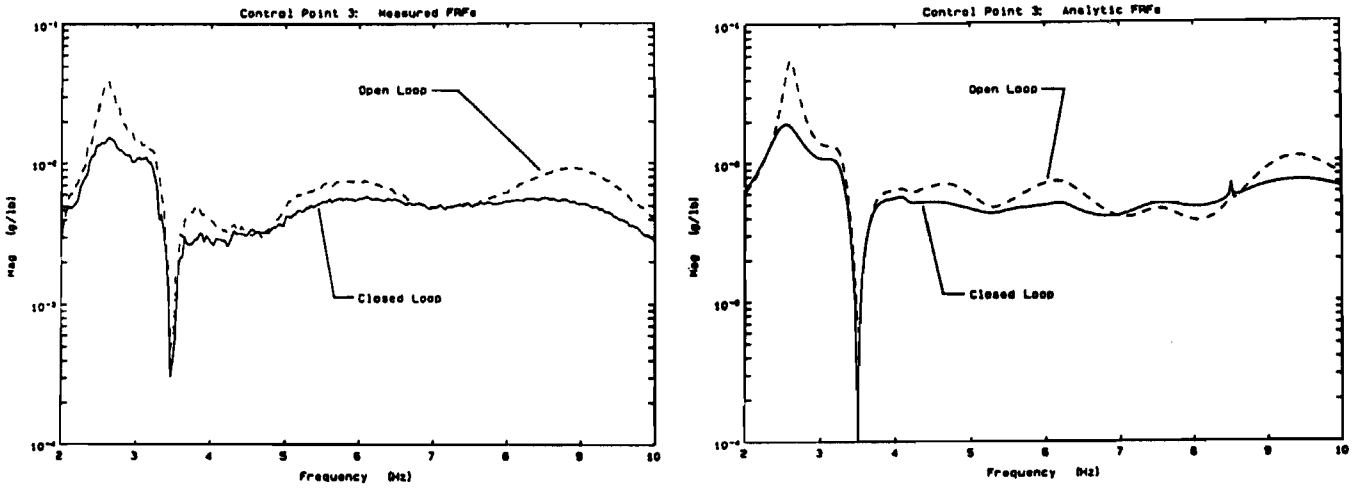

Figure 18 Open- and Closed-Loop FRFs at Control Point 3

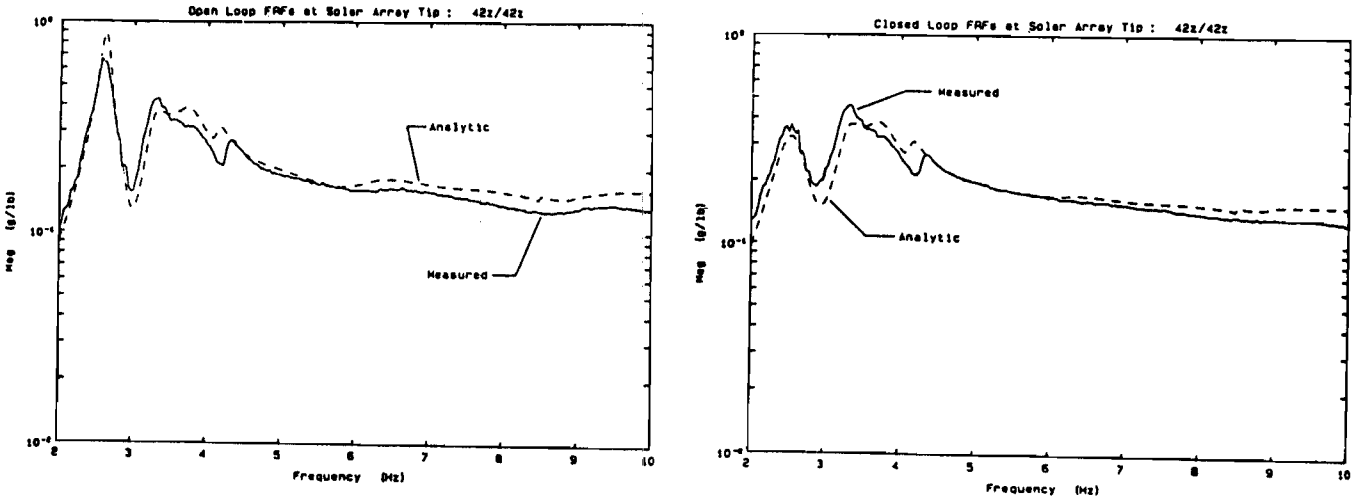

Figure 19 Open- and Closed-Loop FRFs at Solar Array Tip

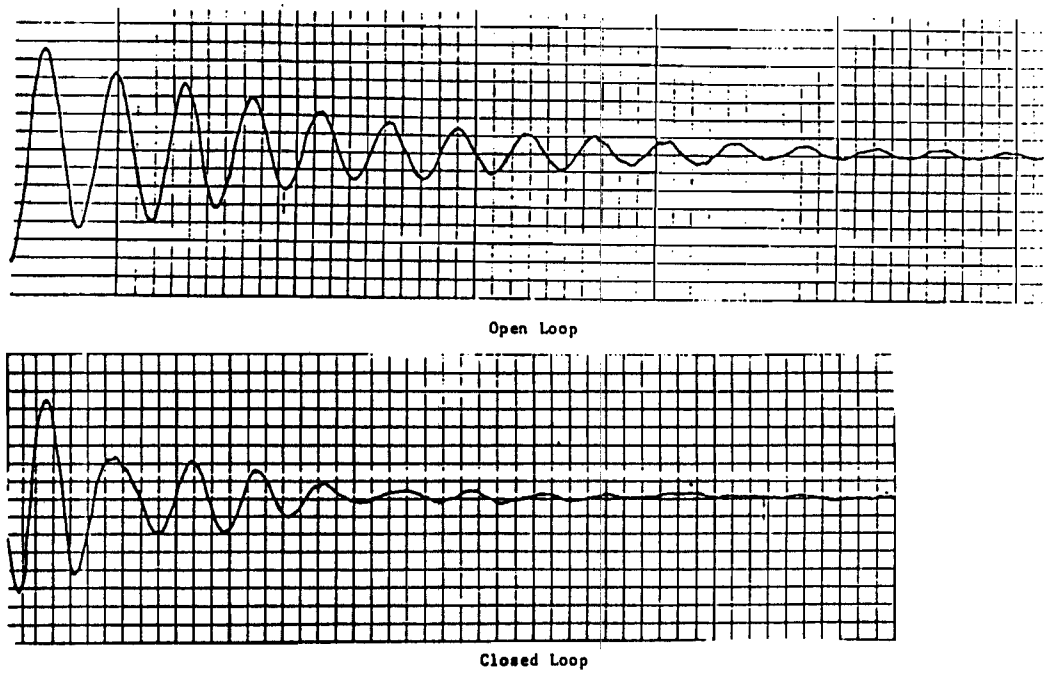

Figure 20 Open- and Closed- Loop Decay Traces

CONCLUSIONS

The modal survey of the Dynamic Test Article (DTA) achieved the goal of identifying all significant structural modes in the 1 to 10 Hz frequency range of interest. The test chamber, test setup, and data acquisition system allowed acquisition of a large volume of data at nearly constant temperature, thereby avoiding temperature dependent viscoelastic material property variations. Data quality was very good at excitation points and points of high response level. Also, measurements were repeatable and indicated nearly symmetric behavior of the DTA. During testing, excitation levels were such that many measurements were of too low a level to obtain quality data with the available instrumentation. However, the low response levels correspond to small modal amplitudes and thus are not very important in terms of synthesized mode shape accuracy. Nonetheless, future testing will be improved by using very low noise instrumentation which is good down to 1 Hz.

Parameter identification performed on the measured data was very successful in consistently estimating 11 of the 22 target modes, while achieving moderate accuracy for another 9 modes. However, because of the closely spaced, highly damped character of the DTA modes, significant variation of modal parameters, particularly damping and residues, was seen for several modes. Only two modes were relatively poorly identified. This experience points to the need for application of more sophisticated parameter identification techniques to the DTA data, and perhaps some theoretical development or tailoring of methods specifically for this type of problem. Also, the effect of real world concerns such as noise and nonlinearity in the data, and small phase errors due to instrumentation must be assessed and, if possible, accounted for.

Other issues of concern were control system performance and behavior of the TMDs on the solar arrays. The active control implementation functioned well in concert with the passive damping and produced the expected results. With regard to the TMDs, the particular tuned mass damper design used on the solar array blankets behaved nonlinearly and thereby degraded some measurements. However, the TMD design did successfully damp the blanket modes.

Overall, agreement between the measured and analytic modal parameters is exceptionally good. The DTA is the most dynamically complicated, damped structure to be rigorously modeled and tested, yet the correlation of results is better than achieved in most modal surveys. Perhaps more important than achieving precise agreement with the analysis is the fact that targeted damping levels can indeed be successfully designed into the fundamental modes of complex structures. This was accomplished using both discrete and distributed passive damping approaches.

On a system level, the DTA modal survey demonstrated that high levels of passive damping can be predictably designed into the dynamically complex structures characteristic of future large space systems. Further, passive damping will allow a relatively simple active control system to be focused on only a few modes while greatly improving performance. The demonstrated achievable damping levels will perform quite effectively in improving the dynamic performance of the structure in terms of settling and jitter response. This is shown by Figure 21 which compares open and closed loop line of sight (LOS) transfer functions to that predicted if the DTA possessed the nominal damping of 0.2% (a level typical of precision structures). Benefits to the overall system include reliable, robust performance with lower weight at possible lower cost compared to approaches not using passive damping.

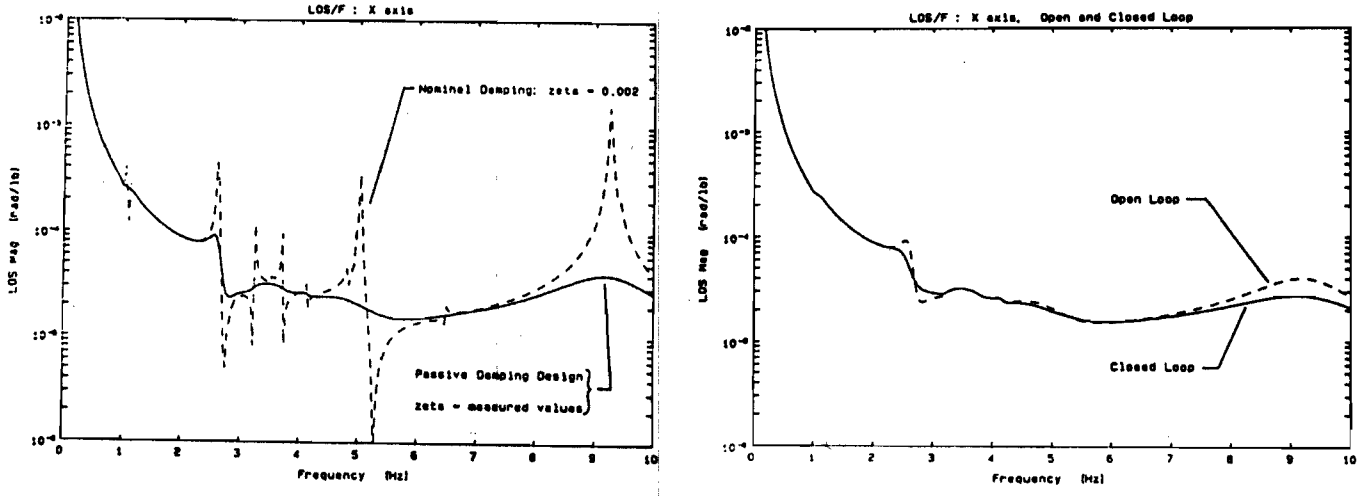

Figure 21 LOS Transfer Functions

ACKNOWLEDGMENT

This work was supported by the Air Force Wright Aeronautical Laboratories under the Passive and Active Control of Space Structures (PACOSS) program, Contract Number F33615-82-C-3222.

REFERENCES

1. Morgenthaler, D. R., and Gehling, R. N., "Design and Analysis of the PACOSS Representative System," Damping 1986 Proceedings, AFWAL-TR-86-3059, Las Vegas, Nevada, 5-7 March 1986.

2. Morgenthaler, D. R., "Passive and Active Damping Techniques Applied to the PACOSS Representative System," to be presented at Damping 1989 Conference, West Palm Beach, Florida, 8-10 February 1989.

3. Morgenthaler, D. R., "Design and Analysis of Passively Damped Large Space Structures," The Role of Damping in Vibration and Noise Control, 1987 ASME Conference on Mechanical Vibration and Noise, Boston, Massachusetts, 27-30 September 1987.

4. Gehling, R. N., "Large Space Structure Damping Treatment Performance," The Role of Damping in Vibration and Noise Control, 1987 ASME Conference on Mechanical Vibration and Noise, Boston, Massachusetts, 27-30 September 1987.

5 Richardson, M. H., and Formenti, D. L., "Parameter Estimation from Frequency Response Measurements Using Rational Fraction Polynomials," 1st International Modal Analysis Conference, Orlando, Florida, November 8-10, 1982.

6 Johnson, C. D., Kienholz, D. A., and Rogers, L. C., "Finite Element Prediction of Damping in Beams with Constrained Viscoelastic Layers," Shock and Vibration Bulletin, No. 50K, Part 1, May 1981.